Applied Catalysis B: Environmental 307 (2022) 121157

Contents lists available at ScienceDirect

Applied Catalysis B: Environmental

journal homepage: www.elsevier.com/locate/apcatb

In-situ production of singlet oxygen by dioxygen activation on iron phosphide for advanced oxidation processes

Ningchao Zheng, Xi He, Ruiting Hu, Ruilin Wang, Quan Zhou, Yekai Lian, Zhuofeng Hu *

School of Environmental Science and Engineering, Guangdong Provincial Key Laboratory of Environmental Pollution Control and Remediation Technology, Sun Yat-sen University, Guangzhou 510006, China

ARTICLE INFO

Keywords:
FeP
Dioxygen activation
Singlet oxygen
Water treatment

ABSTRACT

In this study, we delicately design a novel iron-based dioxygen activation system for sustainable production of $^1O_2$ on iron phosphide (FeP). This is the first time to realize the $^1O_2$ production on Fe-based dioxygen activation. Unlike traditional iron-based materials that only activate dioxygen, this delicately designed FeP can simultaneously activate dioxygen and adsorb some generated •OH. Those •OH can react with $O_2^{\bullet-}$/$HO_2^{\bullet}$. Thus, the •OH-mediated reaction can in-situ occur on the surface of FeP to rapidly produce $^1O_2$. As a result, the FeP exhibits remarkably higher degradation activity for various organic pollutants and pollutants in real aquatic systems in absence of light, electricity and other oxidants. Therefore, this study provides a green strategy to generate $^1O_2$ for environmental remediation and also demonstrates a new role of surface-bound •OH in contributing to the $^1O_2$ production.

1. Introduction

In 1938, H. Kautsky discovered an excited oxygen molecule, singlet oxygen ($^1O_2$) [1]. This is a unique nonradical derivative of oxygen, which is regarded as one of the most potential reactive oxygen species (ROS) [2–5]. Importantly, $^1O_2$ exhibits very high selectivity toward the oxidation of electron-rich pollutants, like pharmaceuticals, unsaturated biomolecules and aromatic organic compounds [6–9]. For example, Xu et al. Reported that the selective oxidation of 5-hydroxymethylfurfural (HMF) to 2,5-furandicarboxylic acid (FDCA) by $^1O_2$, realizing the production of value-added chemicals from renewable resources [10]. Lu et al. Found that the $^1O_2$ produced by MnOx nanosheets in the absence of light can be used for chemodynamic therapy (CDT).[11] Mi et al. Found that the $^1O_2$ generated from peroxymonosulfate oxidation can efficiently degrade several organic pollutants in a wide pH range [12]. Therefore, $^1O_2$ plays an important role in the field of chemical, biomedical and environmental.

The mainstream methods for $^1O_2$ production include: (i) Photosensitization of oxygen by photosensitizers (like molecular dyes or quantum dots) under visible or UV light irradiation.[13–15] (ii) Enzymatic reactions (like peroxidases or oxygenases reaction) in biological intracellular [16,17]. (iii) Electrocatalytic processes (like electrochemical oxidation of lithium carbonate)[18,19]. Although the above methods can produce $^1O_2$, these methods face obvious challenges: (i) The solar light penetration in solution is limited and large-scale industrial application cannot be realized [20]. (ii) Enzymatic reactions can produce $^1O_2$ in a short time, but they rely on intracellular rigorous temperature and special pH conditions [9]. (iii) Electrocatalytic processes hold great potential for $^1O_2$ production, but they require high-intensity energy input [21].

Dioxygen activation systems are always employed to generate ROS for water decontamination [22,23]. These system does not require light, electricity and any other oxidants. One of the most typical representatives is the Fe-based dioxygen activation because Fe is environmentally friendly, inexpensive and highly accessible [24–26]. So far, the ROS produced by Fe-based dioxygen activation has been proved to be •OH or Fe(VI), while barely evidence supported the $^1O_2$ production (Table S1). Thus, it is very interesting to elaborately design a Fe-based dioxygen activation system that can continuously produce $^1O_2$.

It is widely accepted that the $^1O_2$ could be generated via four pathways (Figure S1). (i) The oxidation of $O_2^{\bullet-}$ by high-valent metal cation (Figure S1, route ①) [22,27]. (ii) The recombination of $O_2^{\bullet-}$/$HO_2^{\bullet}$ (Figure S1, route ②) [28,29]. (iii) The Haber-Weiss reaction between $O_2^{\bullet-}$/$HO_2^{\bullet}$ and H_2O_2 (Figure S1, route ③) [30,31]. (iv) The reaction between $O_2^{\bullet-}$/$HO_2^{\bullet}$ and •OH (Figure S1, route ④), this is an •OH-mediated reaction [28,30]. However, the production of high-valent

* Corresponding author.
E-mail address: huzhf8@mail.sysu.edu.cn (Z. Hu).

https://doi.org/10.1016/j.apcatb.2022.121157
Received 17 November 2021; Received in revised form 14 January 2022; Accepted 27 January 2022
Available online 29 January 2022

iron-oxo species (Fe(VI)) only occurs under alkaline conditions [32,33]. The Haber-Weiss reaction between $O_2^{\bullet-}/HO_2^{\bullet}$ and H_2O_2 is also difficult to occur due to its low reaction rate constant (0.13 $-3\ M^{-1}s^{-1}$) [28,34]. Therefore, the recombination of $O_2^{\bullet-}/HO_2^{\bullet}$ and the •OH-mediated reaction should be promising strategies for $^1O_2$ production on Fe-based dioxygen activation. However, to produce $^1O_2$, the $O_2^{\bullet-}/HO_2^{\bullet}$ or •OH needs to contact each other. In homogeneous system, this is not easy to occur because of the short lifetime of radicals (ns~μs level) [11,35]. In our opinion, the recombination of $O_2^{\bullet-}/HO_2^{\bullet}$ or •OH-mediated reaction requires an active site so that the two radicals can fully contact [36,37]. Therefore, there is an urgent need to develop a material that can provide active sites for radical adsorption, reaction and $^1O_2$ production.

Iron phosphide (FeP) belongs to transition metal phosphide, and its structure is unique from other iron-based materials [38]. Specifically, there are two low-valence irons in FeP, one is the common Fe^{2+}, and the other is the unique $Fe^{\alpha+}$ ($0 < \alpha + < 2$) [39,40]. $Fe^{\alpha+}$ is highly similar to metallic Fe but carries partial positive charges, which can provide electrons for reduction reaction [41]. As a result, both Fe^{2+} and $Fe^{\alpha+}$ in FeP can provide electrons for dioxygen activation. Importantly, iron-based materials are prone to produce surface-bound •OH during the Fenton reaction [42,43]. This is because iron-based materials can easily form surface-bound Fe^{2+} on the surface of the material. FeP is a typical Fe-based material, and its surface contains abundant surface-bound Fe^{2+}. Therefore, FeP should be a promising candidate for dioxygen activation, radical adsorption and $^1O_2$ production.

Here, we achieve the production of $^1O_2$ via the •OH-mediated reaction on FeP. This material can provide active sites for radical adsorption and $^1O_2$ production. Tripolyphosphate (TPP), one of the commonly used food additives,[44] is selected to chelate FeP to improve the ability of dioxygen activation. As a result, the FeP/TPP system is capable to activate dioxygen and in-situ producing ROS, especially for $^1O_2$. It is discovered that some •OH produced by FeP/TPP system could be adsorbed on the FeP surface. Then, the FeP triggers a surface-bound •OH mediated reaction to produce $^1O_2$. This is the first time to realize the $^1O_2$ production on Fe-based dioxygen activation. Importantly, unlike other reaction systems that require light, electricity and other oxidants (H_2O_2, persulfate or peroxymonosulfate) (Table S2). The FeP/TPP system only requires aeration, thus, this is a green route for $^1O_2$ production. When applied to advanced oxidation processes (AOPs), the FeP/TPP system also exhibits an excellent degradation activity for various organic pollutants. Hence, the novel FeP/TPP system demonstrates a great potential for green oxidation in chemical synthesis and environmental remediation.

2. Experimental section

2.1. Preparation of FeP

The α-Fe_2O_3 as the precursor of the FeP was prepared first. $FeCl_3$ (64.8 mg), Na_2SO_4 (1.5 mg), $NaH_2PO_4{\cdot}H_2O$ (0.5 mg) and 20 mL of ultrapure water were mixed. After 10 min of vigorous stirring, the mixture was transferred into a 25 mL Teflon-lined stainless steel autoclave and hydrothermally treated at 200 °C for 12 h. Then filtered, washed and dried at 80 °C to obtain purified α-Fe_2O_3.

The FeP was prepared as follows. α-Fe_2O_3 (100 mg) and $NaH_2PO_2{\cdot}H_2O$ (600 mg) were mixed and grounded to fine powder. Subsequently, the powder was calcined at (300−400) °C for 2 h in a flowing N_2 atmosphere. After the products were grounded, the samples were dispersed in 300 mL of ultrapure water, stirred for 1 h, filtered, washed and dried in a vacuum oven at 60 °C for 12 h. Samples FeP-300, FeP-350 and FeP-400 were denoted when the calcined temperatures were 300, 350 and 400 °C, respectively. The chemicals and characterizations used in this study are described in Text S(1−2).

2.2. Experimental procedure

The degradation of pollutants (including ibuprofen (IBU), norfloxacin (NFX), methyl blue (MB) and rhodamine B (RhB)) were tested with a 100 mL glass reactor at 25 °C. In a typical experiment, a certain amount of TPP was dissolved into 60 mL of solution containing 10 ppm pollutants. Before the reaction started, the initial pH was adjusted to desired values using 0.1 M H_2SO_4 and 0.1 M NaOH. Then, a certain amount of FeP sample was added to initiate the degradation reaction with the bubbling air (200 mL/min). At given time intervals, 1 mL of the suspension was taken out and quenched with methanol immediately, and then the suspension was filtered with 0.22 μm membrane for analysis.

2.3. Analyze methods

The concentrations of IBU, NFX and furfuryl alcohol (FFA) were determined by a high performance liquid chromatographer (HPLC, Thermo scientific ultimate 3000) (Table S3). The concentrations of MB and RhB were monitored by an UV–vis spectrometer (UV-2600, Shimadzu). The concentration of Fe^{2+} was detected using a modified 1,10-Phenanthroline spectrophotometric method [42]. The total Fe concentration was analyzed by the same procedure, except for the addition of hydroxylamine hydrochloride to reduce the Fe^{3+} in the system to Fe^{2+} [45]. The diformazan produced by the reaction of NBT (Nitro blue tetrazolium chloride, $O_2^{\bullet-}$ probe) with $O_2^{\bullet-}$ was conducted at the wavelength of 530 nm and was used to qualitatively analyze the $O_2^{\bullet-}$ content in the solution [46,47]. In detail, in the FeP/TPP system, we replaced 10 ppm of IBU with 0.1 mM NBT. Other conditions are consistent with the degradation of IBU in the FeP/TPP system. At given time intervals, 2 mL of the suspension was taken out and filtered with 0.22 μm membrane. The filtrate was measured with a spectrophotometer (UV-2600, Shimadzu). The in-situ generated H_2O_2 was quantified by the colorimetric method using N,N-diethyl-1,4-phenylene-diamine sulfate [48]. The production of •OH was monitored by the coumarin method [49]. The formed active radicals were identified by a Bruker A300 electron paramagnetic resonance (EPR) spectrometer using DMPO (5,5-dimethyl-1-pyrroline-N-oxide) and TEMP (2,2,6,6-tetramethylpiperidine) as a probe. In detail, EPR spectra for the detection of $O_2^{\bullet-}$ in the presence of DMPO, using methanol as the solvent; EPR spectra for the detection of •OH in the presence of DMPO, using water as the solvent; EPR spectra for the detection of $^1O_2$ in the presence of TEMP, using water as the solvent. The intermediate products of FFA oxidized by $^1O_2$ or •OH was detected by UHPLC/MS, the detailed results can be seen in Text S3.

3. Results and discussion

3.1. Material characterization

The XRD is measured to investigate the crystal structures of synthesized samples (Fig. 1a). The pattern of α-Fe_2O_3 with the diffraction peaks at 2θ = 24.1°, 33.2°, 35.6°, 49.5°, 54.1°, 62.5° and 64.0° are attributed to the (012), (104), (110), (024), (116), (214) and (300) planes of the hematite (PDF#33–0664), respectively. However, the intensity of characteristic peaks of α-Fe_2O_3 decreases and several new peaks appear from α-Fe_2O_3 to FeP-300. The new diffraction peaks at 2θ = 40.2°, 44.2°, 47.3°, 52.9° and 54.6° are ascribed to the (111), (201), (210), (002) and (211) planes of the barringerite (Fe_2P: PDF#51–0943), respectively. This is because the Fe^{3+} in α-Fe_2O_3 is partially reduced to Fe^{2+} and part of the oxygen atoms are replaced by phosphorus. When the phosphidation temperature increase to 350 °C (FeP-350), the diffraction peaks of α-Fe_2O_3 completely disappear and some new peaks appear. The new characteristic peaks at 2θ = 32.7°, 34.5°, 37.1°, 48.3°, 56.1° and 59.6° are assigned to the (011), (200), (111), (211), (031) and (002) planes of orthorhombic FeP (PDF#39–0809), indicating that the

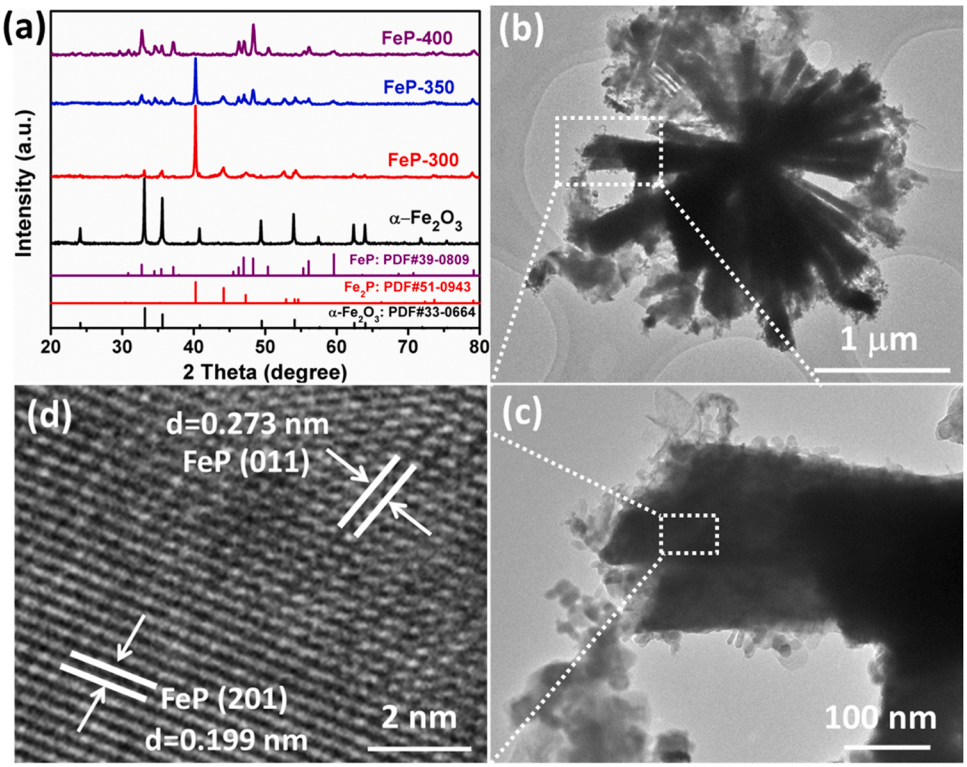

Fig. 1. (a) The XRD patterns of α-Fe_2O_3, FeP-300, FeP-350 and FeP-400. (b) TEM image of FeP-400. (c, d) HRTEM images of FeP-400.

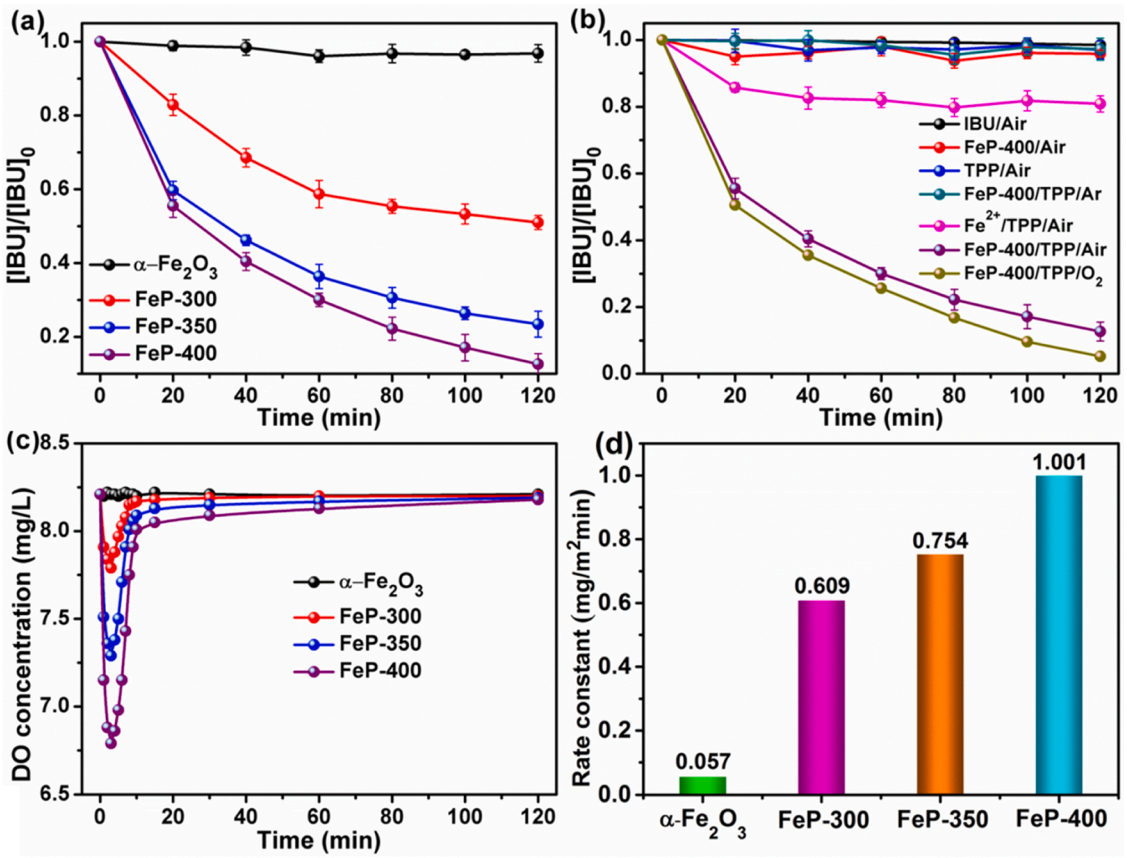

Fig. 2. (a) IBU degradation by four samples. (b) IBU degradation by seven control experiments. (c) The dissolved oxygen variation during the degradation of IBU by four samples. (d) The normalized apparent rate constant of the degradation per unit surface area over four samples. Reaction conditions: [IBU] = 10 ppm; [TPP] = 2 mM; pH = 6.0; [sample] = 0.2 g/L; [Fe^{2+}] = 78 μM; air-bubbled.

crystal phase of FeP-350 coexistence of Fe_2P and FeP. Further to increase the phosphidation temperature reaches 400 °C (FeP-400). The crystal structure of FeP-400 is only composed of FeP, no additional impurity peaks are observed, suggesting that the high purity of FeP is successfully synthesized. These results indicating that the crystal phase of α-Fe_2O_3 is firstly converted to Fe_2P, then to FeP during the phosphidation process (Figure S2).

Figure S3a shows the synthesized α-Fe_2O_3 is uniform and cylinder-like with a concave center. Figure S3(b-d) show the morphology of phosphidated α-Fe_2O_3 at different temperatures. It can be seen that as the degree of phosphidation deepens, the morphology of α-Fe_2O_3 change from the cylinder-like with a concave center to the rod finally transformed into fan structure. Fig. 1b exhibits the TEM image of FeP-400. The morphology of FeP-400 observed from TEM image is consistent with the SEM image (Figure S3d). The HRTEM images in Fig. 1(c-d) show that the lattice spacing of FeP-400 is 0.199 nm and 0.273 nm, corresponding to the (201) and (011) plane of orthorhombic FeP, respectively. Indicating that the high purity of FeP is prepared and in line with the XRD result. The N_2 adsorption-desorption isotherms are shown in Figure S4, from which Brunner-Emmet-Teller (BET)-specific surface areas are calculated to be 5.02 m^2/g (α-Fe_2O_3), 9.13 m^2/g (FeP-300), 15.12 m^2/g (FeP-350) and 16.35 m^2/g (FeP-400), and the average pore sizes are 4.82 nm, 7.23 nm, 8.44 nm and 8.27 nm, respectively (Table S4).

3.2. Activation of dioxygen for IBU degradation

The prepared four samples are used to degrade IBU (Fig. 2a). The IBU degradation rates are 3.2%, 49.4%, 77.1% and 87.5% for α-Fe_2O_3, FeP-300, FeP-350 and FeP-400 within 120 min, respectively. It shows that the IBU degradation efficiency is boosted for samples with the elevating temperature of phosphidation. However, when the phosphidation temperature reaches 450 °C, it can be seen that the sample of FeP-450 contains impurity of $Fe(PO_3)_3$ and FeP (Figure S5a). As a result, the IBU degradation efficiency decreased from 87.5% (FeP-400) to 79.1% (FeP-450) (Figure S5b). This result indicates that the FeP-400 is the optimal sample for IBU degradation.

Generally, it may be argued that IBU will be lost because it may be adsorbed or volatilized due to aeration. Seven control experiments are performed (Fig. 2b). In the control system of FeP-400/TPP/Ar, there is no oxygen for dioxygen activation. It can be seen that the IBU concentration did not change within 120 min, indicating that the loss of IBU by adsorbed is negligible. Second, the result of IBU/Air system suggests that the loss of IBU by aeration is insignificant. Third, the results of TPP/Air and FeP-400/Air systems indicate that TPP or FeP-400 alone could not activate O_2 to degrade IBU. The degradation of IBU by FeP-400 under pure oxygen conditions is also conducted. It can be seen that the degradation rate of IBU under pure oxygen conditions is better than that of air conditions. This is because the FeP-400 reacts with oxygen more easily under pure oxygen conditions. As a result, the degradation rate of IBU increases. Fig. 2c shows the changes in dissolved oxygen (DO) during the reaction of four samples. It can be observed that the concentration of DO decreased rapidly once the reaction began, further confirming that O_2 is quickly activated by FeP-400 in the presence of TPP. Due to the continuous aeration, the concentration of DO recovered gradually after 5 min

It is also highly important to evaluate the activity of samples by normalizing the surface area of samples (Eq. 1). The normalized apparent rate constants according to per unit specific surface area are calculated to be 0.057 mg/(m^2·min), 0.609 mg/(m^2·min), 0.754 mg/(m^2·min) and 1.001 mg/(m^2·min) for α-Fe_2O_3, FeP-300, FeP-350 and FeP-400, respectively (Fig. 2d). These results also reveal that the FeP-400 has the maximum degradation density (mg/m^2·min) for IBU. The pH of the solution increases slightly with the reaction goes on (Figure S6). The result is consistent with previous literature about the activation of dioxygen without buffering.[26] It can be explained by the accumulation of OH^- due to the H^+ consumption for in-situ generation of H_2O_2.[50,51].

$$\text{Normalized apparent rate constants} = \frac{degradation\ \ rate\ \ constant\ \ (min^{-1})}{BET\ \ surface\ \ area\ \ (m^2/g)} \quad (1)$$

When the degradation reaction is demonstrated, it is necessary to explore the effect of FeP-400 dosage and TPP dosage on the catalytic activity of FeP-400/TPP/Air system. As seen in Figure S7, the optimized dosage of FeP-400 and TPP are 0.2 g/L and 2 mM, respectively. Therefore, 0.2 g/L of FeP-400 and 2 mM of TPP are selected as the optimal dosage for the following experiments. The detailed results and discussion can be seen in Text S4.

3.3. Heterogeneous activation of dioxygen for IBU degradation

It is necessary to study whether the activation process involves aqueous Fe^{2+} released from the sample. Thus, the concentrations of leached Fe^{2+} during these four samples are investigated. As shown in Figure S8 and Fig. 3a, leaching of Fe^{2+} is not detected in the α-Fe_2O_3/TPP/Air system. However, in other three systems (FeP-300, FeP-350 and FeP-400), the concentration of leached Fe^{2+} increased within 20 min after adding sample to initiate the degradation reaction. However, with time prolongs, the concentration of leached Fe^{2+} gradually decreased until the reaction is over. This finding is mainly attributed to the oxidization of leached Fe^{2+} to Fe^{3+} via the dioxygen activation process. Thus, the leached total Fe ion concentration increases steadily (Figure S9 and Fig. 3b). This result indicates that the leached Fe^{2+} contributes to the dioxygen activation for IBU degradation to some extent.

However, we find that Fe leaching is not the main reason for IBU degradation in the FeP-400/TPP/Air system. Here, homogenous dioxygen activated by the same amount of total leached Fe is carried out. The maximum leaching amount of total dissolved Fe in FeP-400/TPP/Air system is 78 μM within 120 min (Fig. 3b). This 78 μM is the accumulated concentration of total leaching Fe rather than instantaneous concentration. Therefore, this suggests that low Fe ions leaching rate. In our control experiment, FeP-400 is replaced by 78 μM $FeSO_4$, and the degradation efficiency of IBU decreases remarkably from 87.5% to 19.2% (Fig. 2b). This strongly indicates that the contribution of homogeneous dioxygen activation by dissolved Fe^{2+} derived from FeP-400 only accounts for a small section. In this case, the consumption of H_2O_2 in FeP-400/TPP/Air system is mainly affected by FeP-400 rather than the Fe^{2+} in the solution. Also, in this homogeneous situation, no $^1O_2$ is formed, confirming that the $^1O_2$ is not produced in homogeneous process. This will be discussed in the mechanism section below.

Moreover, another control experiment is performed by fixing the pH at 2, 4, 6 and 8 (Fig. 3c). Generally, better IBU degradation would be obtained under lower pH. This is because low pH not only inhibits the Fe ion precipitation but also accelerates the Fe^{2+} leaching from the sample, which implied that dioxygen would be activated faster to generate ROS. However, even the concentration of leached Fe^{2+} in pH 2 reaches 273 μM within 120 min (Figure S10 and Fig. 3d), the IBU degradation efficiency is only 31% (Fig. 3c). This result is mainly due to the negatively charged $P_3O_{10}^{5-}$ ions (TPP) reacts with a large amount of H^+ to form $H_5P_3O_{10}$ at pH2,[46] which reduces the complexing ability of TPP with FeP-400 and further reduces the degradation efficiency of IBU. Additionally, when the pH of reaction solution is fixed at 8, the concentration of Fe^{2+} in solution is very low (Fig. 3d). It is below the quantification limit of the widely-used 1,10-phenanthroline colorimetric method (0.02 mg L^{-1}) [52,53]. Under the circumstance, the FeP-400/TPP/Air system can still contribute to the IBU degradation of about 58% (Fig. 3c). These results demonstrate that the heterogeneous dioxygen activation plays a dominant role for IBU degradation in FeP-400/TPP/Air system.

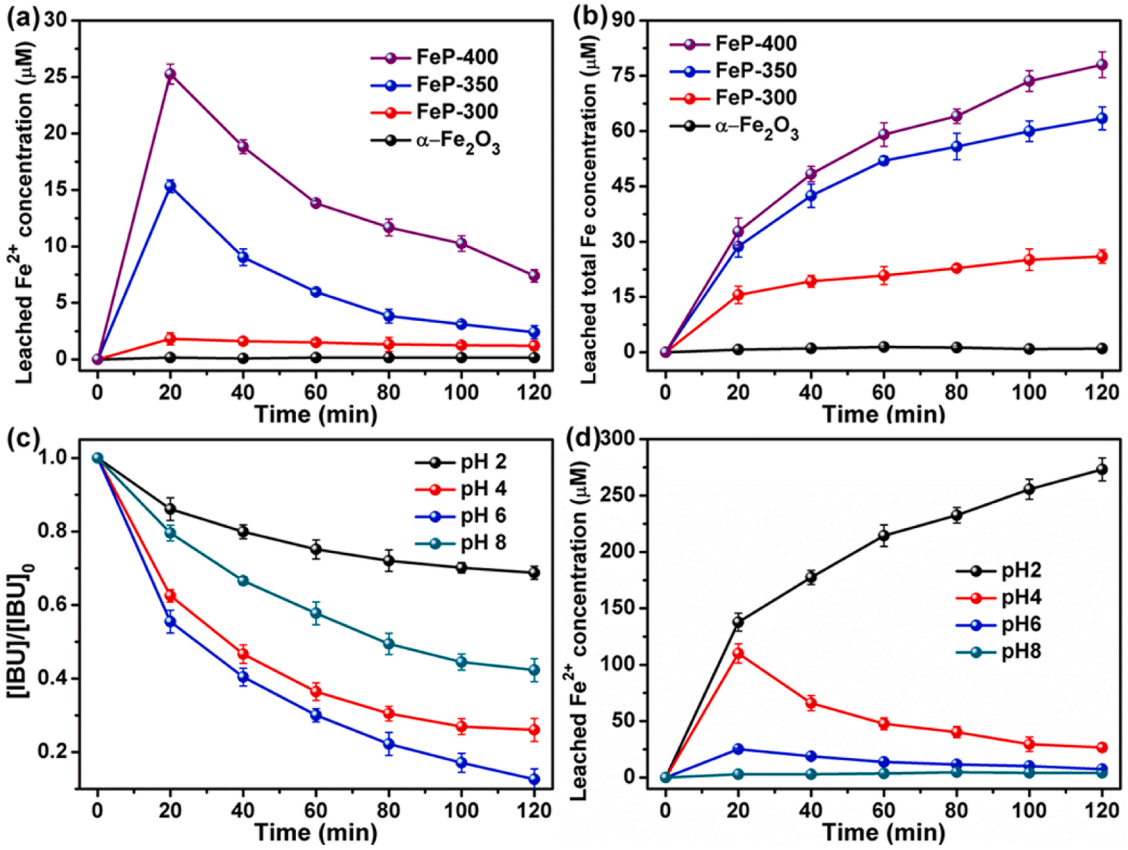

Fig. 3. The concentrations of leached (a) Fe^{2+} and (b) total Fe in different samples during the IBU degradation. (c) Effect of pH on the degradation of IBU by FeP-400 and (d) the concentrations of leached Fe^{2+} in different pH during the IBU degradation. Reaction conditions: [IBU] = 10 ppm; [TPP] = 2 mM; pH = 6.0; [sample] = 0.2 g/L; air-bubbled.

3.4. Exploration of the spontaneous formation of ROS on FeP-400

To identify the content of ROS in the FeP-400/TPP/Air system, three groups of probe experiments are designed. It is known that nitro blue tetrazolium chloride (NBT) could be used to detect $O_2^{\bullet-}$. It does not react with other ROS or react with Fe^{2+} (Figure S11). It only reacts with

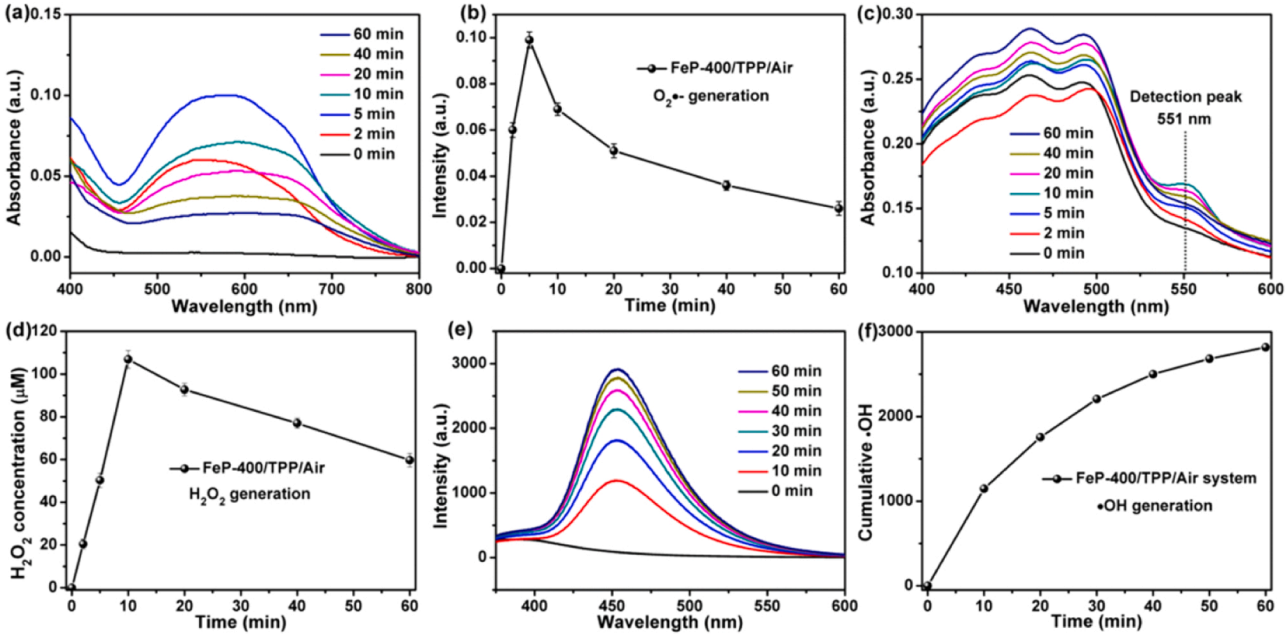

Fig. 4. (a, b) Detection of $O_2^{\bullet-}$ generation on FeP-400/TPP/Air system by spectrophotometry at 530 nm (NBT = 0.1 mM). (c, d) Detection of H_2O_2 generation on FeP-400/TPP/Air system by spectrophotometry at 551 nm ([IBU] = 10 ppm). (e, f) Detection of cumulative •OH generation on FeP-400/TPP/Air system by photoluminescence spectra at 460 nm (coumarin =1 mM). Reaction conditions: [TPP] = 2 mM; pH = 6.0; [sample] = 0.2 g/L; air-bubbled.

$O_2^{\bullet-}$ to produce diformazan, which has a characteristic absorption wavelength at 530 nm.[46] Fig. 4(a, b) exhibit that $O_2^{\bullet-}$ is generated in large quantities at beginning of the reaction and reaches its maximum concentration at 5 min. However, with time prolongs, the concentration of $O_2^{\bullet-}$ gradually decreases until the end of the reaction. This result indicates that $O_2^{\bullet-}$ plays a vital intermediate in the system, and the decrease after 5 min is ascribed to the conversion of $O_2^{\bullet-}$ to other species rapidly, such as H_2O_2. Not surprisingly, Fig. 4(c, d) show that the concentration of generated H_2O_2 gradually increases within 10 min, but decreases gradually with the time prolongs. It is possible that the generated H_2O_2 is rapidly consumed via the Fenton reaction with FeP-400 in the system, resulting in the concentration of H_2O_2 decreases after 10 min. To further investigate the generation of •OH, the photoluminescence signal of 7-hydroxycoumarin formed by coumarin capturing •OH is measured. As shown in Fig. 4(e, f), the signal of 7-hydroxycoumarin increases gradually, indicating that the generation of •OH in the FeP-400/TPP/Air system.

To further evaluate the contribution of different ROS on IBU degradation, a series of sacrificial experiments are conducted. It is widely accepted in the literature that superoxide dismutase (SOD), catalase (CAT), *tert*-butyl alcohol (TBA) and 2,2,6,6-tetramethylpiperidine (TEMP) are quencher for $O_2^{\bullet-}$, H_2O_2, •OH and $^1O_2$, respectively [25, 27,54]. As shown in Fig. 5a, the addition of SOD inhibits the IBU degradation completely, suggesting that the $O_2^{\bullet-}$ is the first formed radical in FeP-400/TPP/Air system. In the presence of CAT and TBA, the IBU degradation rates decreased by 84.4% and 79.8%, respectively, suggesting H_2O_2 and •OH contribute to the IBU degradation. Besides, in the presence of TEMP, the IBU degradation rate is also notably decreased from 87.5% to 16.6% in 120 min. The strong inhibitory effect of TEMP proves that the $^1O_2$ generated in the FeP-400/TPP/Air system plays an important role in the degradation of IBU. It may be argued that TEMP can also quench •OH, but we can prove that the inhibition effect of TEMP on •OH is much weaker than that of TBA. As shown in Figure S12, less •OH is captured by TEMP than TBA in the traditional Fenton reaction (Fe^{2+}/H_2O_2). The dosage of TBA and TEMP in Fe^{2+}/H_2O_2 system is consistent with FeP-400/TPP/Air system. Therefore, the FeP-400/TPP/Air system must produce $^1O_2$ and contribute to the degradation of IBU.

EPR spectra are employed to further investigate the existence of $^1O_2$ in FeP-400/TPP/Air system. DMPO and TEMP are used as spin-trapping reagents for the capture of $O_2^{\bullet-}$/•OH and $^1O_2$, respectively. Interestingly, it can be seen that the weak $O_2^{\bullet-}$ and •OH signal, but robust $^1O_2$ signal is detected in FeP-400/TPP/Air system (Fig. 5(b-d)). This indicates that $^1O_2$ is the main ROS in the FeP-400/TPP/Air system. The weak EPR signal of $O_2^{\bullet-}$ and •OH should be attributed to the rapid conversion of $O_2^{\bullet-}$ and •OH to $^1O_2$ in the FeP-400/TPP/Air system, which corresponds to the •OH-mediated reaction. This will be discussed in the mechanism section below.

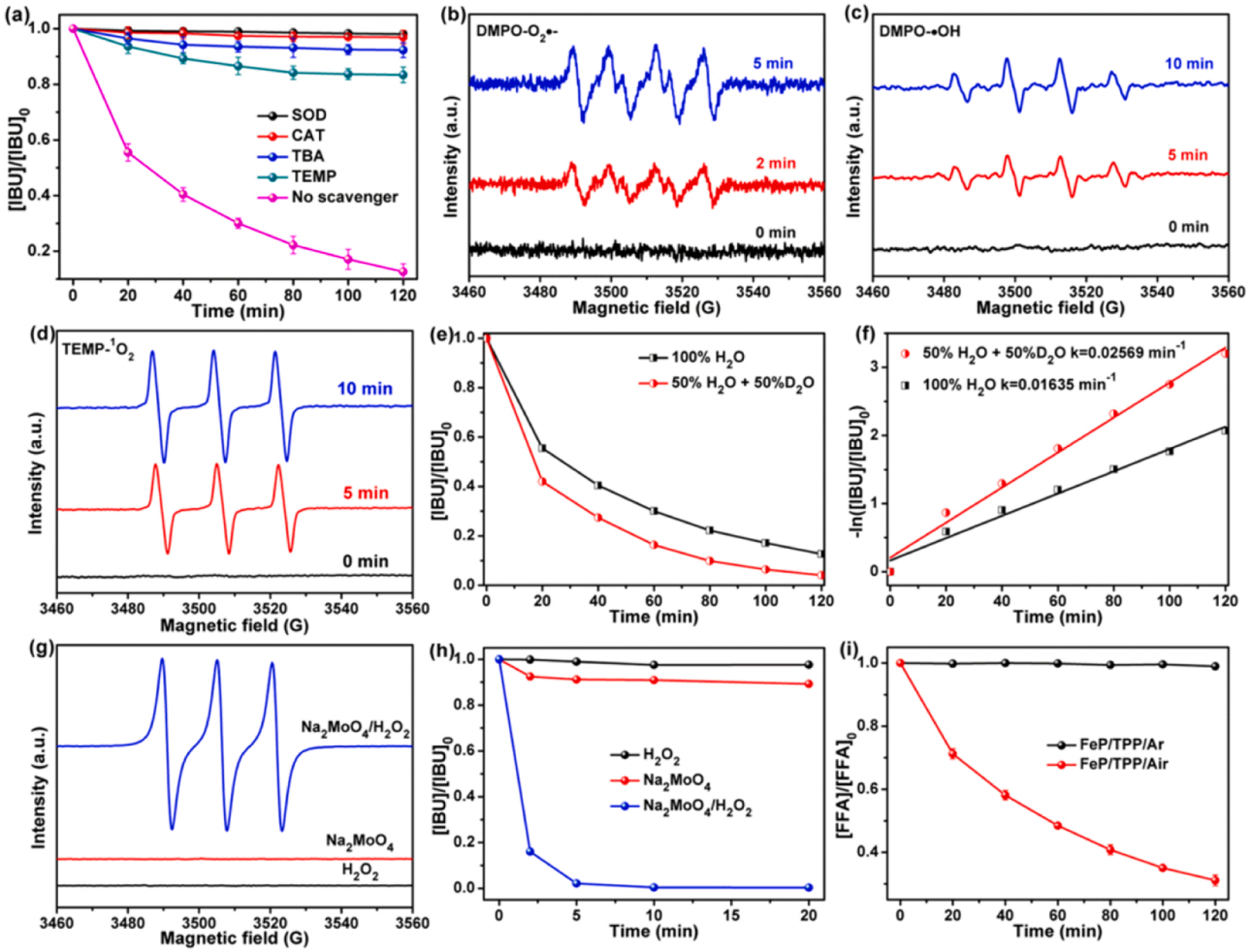

Fig. 5. (a) The inhibition effect of different radical scavengers on IBU degradation in FeP-400/TPP/Air system (SOD for $O_2^{\bullet-}$, CAT for H_2O_2, TBA for •OH, TEMP for $^1O_2$). EPR spectra of (b) DMPO-$O_2^{\bullet-}$, (c) DMPO-•OH and (d) TEMP-$^1O_2$ adducts formed in FeP-400/TPP/Air system. (e) IBU degradation in FeP-400/TPP/Air system under different solvents. (f) Plots of –ln([IBU]/[IBU]$_0$) versus time for IBU degradation in FeP-400/TPP/Air system under different solvents. (g) EPR spectra of TEMP-$^1O_2$ in Na_2MoO_4/H_2O_2 system (pH=10). (h) Degradation of IBU by Na_2MoO_4/H_2O_2 system (pH=10). (i) FFA degradation in FeP-400/TPP/Air system. Reaction conditions: [IBU] = 10 ppm; [TPP] = 2 mM; pH = 6.0; [sample] = 0.2 g/L; [Na_2MoO_4] = 0.1 M; [H_2O_2] = 0.5 M; [FFA] = 115 μmol/L; air-bubbled.

The domination of $^1O_2$ is further confirmed by quantitative measurements. Because $^1O_2$ exhibits kinetic solvent isotopic effect (KSIE), the quenching rate constants of $^1O_2$ by H_2O and D_2O are 2.5×10^5 and 1.6×10^4 $M^{-1}S^{-1}$, respectively.[55] This means that the consumption of $^1O_2$ is approximately 15.6 times slower in pure D_2O than that in pure H_2O. Thus, the degradation rate constant of IBU by $^1O_2$ in a solution containing D_2O can be calculated according to Eq. (2).

$$k_{obs,\ H2O,\ D2O} = \frac{k_{H2O} \times k_{obs,\ H2O}}{x_{H2O} \times k_{H2O} + x_{D2O} \times k_{D2O}} \quad (2)$$

where xH_2O and xD_2O represent the molar fraction of H_2O and D_2O, respectively. $k_{obs,H2O}$ represents the corresponding IBU degradation rate constant in 100% H_2O. k_{H2O} and k_{D2O} are 2.5×10^5 and 1.6×10^4 $M^{-1}S^{-1}$, respectively.[56] The pseudo-first-order rate constants for IBU degradation in 100% H_2O is determined to be 0.01635 min^{-1} (Fig. 5(e, f)). According to Eq. (2), if the IBU degradation is only attributed to $^1O_2$, $k_{obs,H2O,D2O}$ in 50% D_2O is 0.03073 min^{-1}. However, this value is determined to be only 0.02569 min^{-1} (Fig. 5f). As a result, it can be calculated that $^1O_2$ contributed 64.9% of the total IBU degradation.

The degradation of IBU by $^1O_2$ is also confirmed. According to the literatures,[57–59] $^1O_2$ can be selectively and quantitatively generated in alkaline water through the disproportionation of H_2O_2 catalyzed by molybdate ions (Eq. 3). In this case, only $^1O_2$ is produced. Therefore, if IBU is degraded in the Na_2MoO_4/H_2O_2 system, the degradation can be attributed to $^1O_2$. Fig. 5g shows the Na_2MoO_4/H_2O_2 system produces a large amount of $^1O_2$. Fig. 5h shows the Na_2MoO_4/H_2O_2 system can quickly degrade IBU. These results solidly prove that IBU can be effectively degraded by $^1O_2$.

$$2H_2O_2 \longrightarrow^{MoO_4^{2-}} 2H_2O + {}^1O_2(100\%) \quad (3)$$

Besides, $^1O_2$ generation is further confirmed by furfuryl alcohol (FFA) probe, which is high activity to $^1O_2$ with a rate constant of 1.2×10^8 M^{-1} S^{-1}.[60] It can be seen that near 70% degradation of FFA (115 μM) is achieved (Fig. 5i). It may be argued that the FFA could be oxidized by •OH. To exclude this, an LC-MS with electron spray ionization (ESI) source is employed to identify the intermediate products. According to previous reports,[61,62] the intermediate products from the oxidation of FFA by $^1O_2$ include three typical substances (Figure S13), including $C_5H_6O_3$ (*m/z* 112.9691), $C_5H_6O_4$ (*m/z* 129.9581) and $C_4H_4O_3$ (*m/z* 98.9948). In the FeP-400/TPP/Air system, those three important typical products are detected at the retention time of 1.122, 0.856 and 3.746 min, respectively (Figure S13). Although FFA can also be considered to be degraded by •OH (Figure S14a), the intermediate products of FFA degraded by •OH are completely different from those degraded by $^1O_2$ (Figure S14b). No those three typical products can be found if FFA is degraded by •OH. This result is consistent with the previous studies and indicating that a constant in-situ production of $^1O_2$ in the FeP-400/TPP/Air system.

3.5. Investigation of the mechanism for $^1O_2$ production

3.5.1. The function of TPP

The concentration of TPP during the degradation process is also investigated by ion chromatography. Fig. 6a shows the adsorption capacity of TPP in the FeP-400/TPP/Air system gradually increases, suggesting that the portion of TPP is adsorbed on the surface of FeP-400. Fig. 6b exhibits the absorbance of TPP, FeP-400 and FeP-400/TPP. It can be seen that the absorbance of FeP-400/TPP at 275 nm is much higher than that of individual TPP or FeP-400 at the same condition, indicating that a strong complexation between TPP and FeP-400. It may

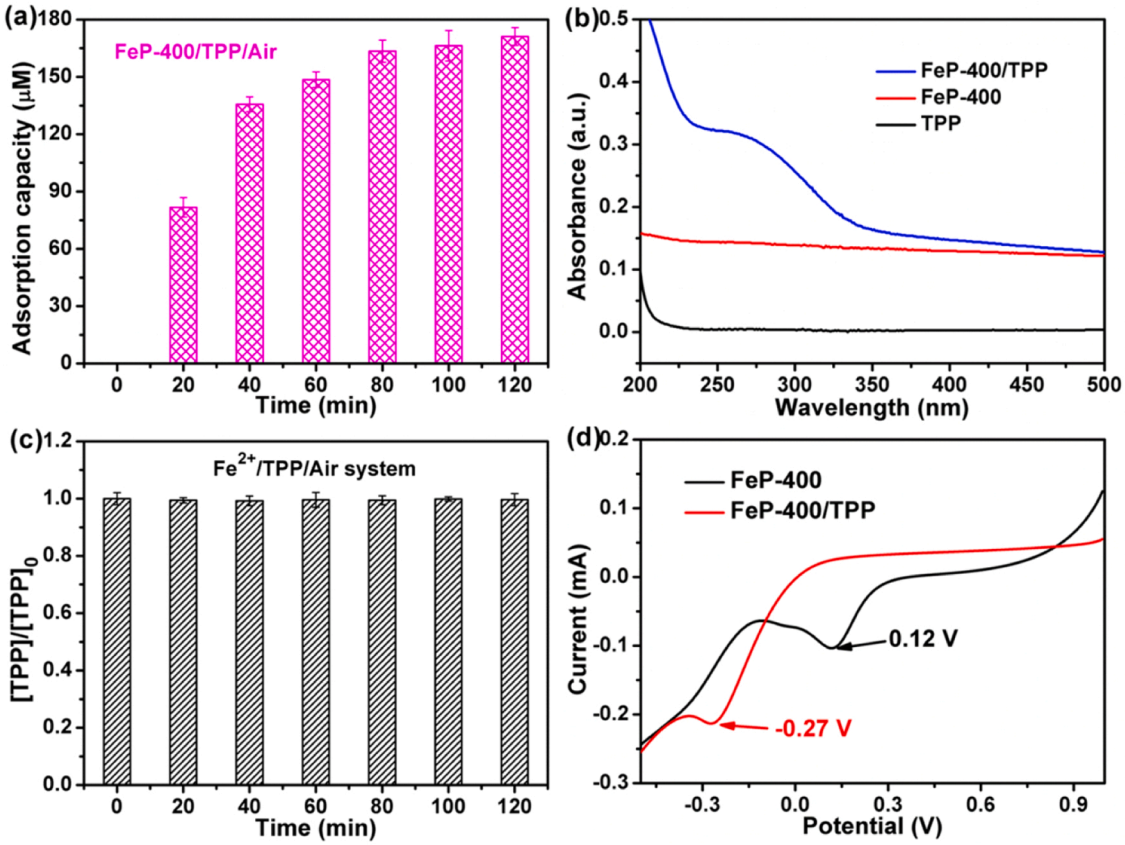

Fig. 6. (a) The adsorption capacity of TPP onto FeP-400 during the degradation process. (b) UV–vis spectrum of TPP, FeP-400 and FeP-400/TPP. (c) The variation of TPP concentration during the degradation process in Fe^{2+}/TPP/Air system. (d) Linear sweep voltammetry of FeP-400 and FeP-400/TPP. Reaction conditions: [IBU] = 10 ppm; [TPP] = 2 mM; pH = 6.0; [sample] = 0.2 g/L; air-bubbled.

be argued that whether the TPP can be consumed during the degradation process. However, Fig. 6c shows the concentration of TPP in the Fe^{2+}/TPP/Air system always maintains initial concentration during the degradation process, indicating that the TPP is stable and is not consumed.

The function of TPP is further investigated. We find that the adsorption of TPP on the FeP-400 could effectively decrease the redox potential of Fe^{3+}/Fe^{2+} from 0.12 V to − 0.27 V (Fig. 6d). As a result, FeP-400 shows higher reducibility to activate dioxygen and production of $O_2^{\bullet-}$ (Table S5, Reaction 1–3).[47] Then, the $O_2^{\bullet-}$ could quickly be converted to $HO_2^{\bullet}$ with a high rate constant of 1.0×10^{10} $M^{-1}s^{-1}$ (Table S5, Reaction 4).[63] The adsorption of TPP on FeP and the electron transfer between FeP and TPP are also confirmed by Density Function Theory calculation, which indicates that Fe and TPP can be complexed with each other and the TPP is in a triangle model on the surface of FeP. The detailed results and discussion can be seen in Text S5.

3.5.2. *The mechanism for $^1O_2$ production*

According to literature reported, it is accepted that $^1O_2$ could be generated via four pathways (Figure S1): (i) The oxidation of $O_2^{\bullet-}$ by high-valent metal cation (Figure S1, route ①) [22,27]. (ii) The recombination of $O_2^{\bullet-}/HO_2^{\bullet}$ (Figure S1, route ②)[28,29]. (iii) The Haber-Weiss reaction between $O_2^{\bullet-}/HO_2^{\bullet}$ and H_2O_2 (Figure S1, route ③) [30,31.] (iv) The reaction between $O_2^{\bullet-}/HO_2^{\bullet}$ and •OH (Figure S1, route ④), this is the •OH-mediated reaction that can be feasible for $^1O_2$ production [28,30].

However, two possible pathways in our system for $^1O_2$ generation can be excluded: (i) The oxidation of $O_2^{\bullet-}$ by high-valent metal cation for $^1O_2$ generation could be ruled out because the high-valent metal cation (Fe(VI)) are not detected in FeP/TPP/Air system (Figure S17, PMSO method)[64,65]. (ii) The Haber-Weiss reaction between $O_2^{\bullet-}/HO_2^{\bullet}$ and H_2O_2 could also be ruled out because there is only a small amount of H_2O_2 in our system (Fig. 4d), but Haber-Weiss reaction often requires high concentration of H_2O_2 [28]. More importantly, the reaction rate constant of $O_2^{\bullet-}/HO_2^{\bullet}$ and H_2O_2 is about 5–10 magnitude smaller than the $O_2^{\bullet-}/HO_2^{\bullet}$ recombination or •OH-mediated reaction (Table S5, Reaction 7–12).[34] With regarding $O_2^{\bullet-}/HO_2^{\bullet}$ recombination and •OH-mediated reaction, it is speculated that the •OH-mediated reaction is dominant for $^1O_2$ generation due to the reaction constant is higher than that of $O_2^{\bullet-}/HO_2^{\bullet}$ recombination (Table S5, Reaction 9–12). The above speculation can be confirmed by the control experiments. It is well known that TBA could quench overall •OH.[66] Therefore, when TBA is added to the FeP/TPP/Air system, the •OH generated in the system will be quenched and not be converted into $^1O_2$ via •OH-mediated reaction. In fact, when the dosage of TBA is gradually increases from 0 to 0.2 mL, the signal intensity of $^1O_2$ drops sharply (Fig. 7a). These results indicating that the $^1O_2$ generation in FeP/TPP/Air system is mainly attributed to the •OH-mediated reaction.

It may be argued that whether the homogeneous dioxygen activation can also produce $^1O_2$, because the homogeneous dioxygen activation can also generate •OH and $O_2^{\bullet-}$. However, there is no $^1O_2$ signal detected in Fe^{2+}/TPP/Air system (Fig. 7b). This strongly indicates that the $^1O_2$ is formed on the surface of the FeP rather than in the solution. This is reasonable because the reorganisation step requires radicals to contact each other and this is not easy to occur in solution.

It means that heterogeneous reaction is the dominating reaction for $^1O_2$ production. In our opinion, the key step of the •OH-mediated reaction is a process of reorganisation of two radicals (Table S5, Reaction 11–12), and this reorganisation requires an active site so that the two radicals can fully contact.[36] In FeP/TPP/Air system, the surface of FeP acts as the active site for radical adsorption and reorganisation. This can be proved by a control experiment. It is reported that F^- in the solution could desorb •OH bound on material surface by forming a strong hydrogen bond.[42] In this case, the intensity of DMPO trapped •OH EPR signal in FeP/TPP/NaF should be stronger than FeP/TPP. This is because the •OH bound on the surface of the FeP is desorbed by F^-. As expected, the addition of NaF improved the intensity of DMPO trapped •OH EPR signal (Figure S18). Meanwhile, the addition of NaF greatly suppressed the signal intensity of $^1O_2$ (Fig. 7c). This result well validates that the surface-bound •OH is generated in FeP/TPP system and the surface-bound •OH is essential precursors for $^1O_2$ production. Furthermore, it is widely accepted in the literature that potassium iodide (KI)

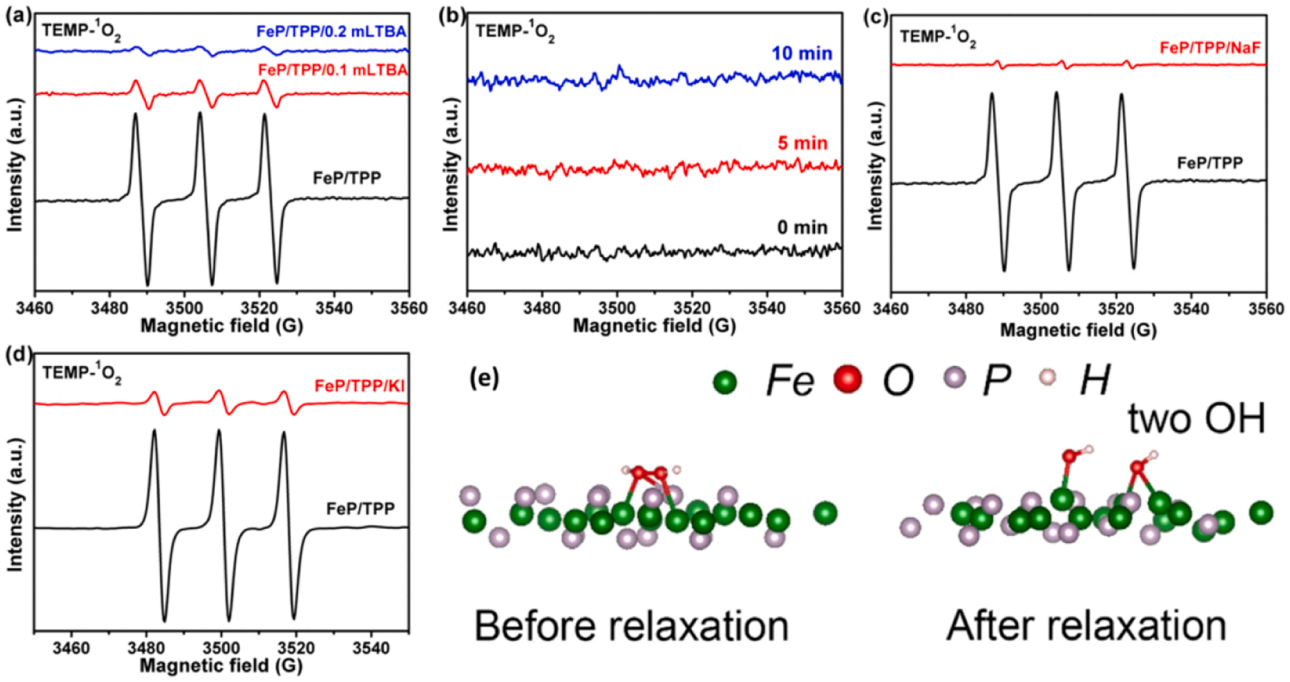

Fig. 7. (a) EPR spectra of TEMP-$^1O_2$ in FeP/TPP/TBA system. (b) EPR spectra of TEMP-$^1O_2$ in Fe^{2+}/TPP/Air system. (c) EPR spectra of TEMP-$^1O_2$ in FeP/TPP/NaF system. (d) EPR spectra of TEMP-$^1O_2$ in FeP/TPP/KI system. (e) The dissociation of H_2O_2 and adsorption of OH on the surface of FeP. Reaction conditions: [IBU] = 10 ppm; [TPP] = 2 mM; pH = 6.0; [NaF] = 0.2 g/L; [KI] = 0.1 g/L; [sample] = 0.2 g/L; air-bubbled.

could quench surface-bound •OH.[43,66] Figure S19 shows the addition of KI to scavenge surface-bound •OH significantly suppresss the reactivity of FeP in IBU degradation (decreased from 87.5% to 16.4%). Fig. 7d shows the addition of KI in FeP/TPP/Air system remarkedly decreases the signal intensity of $^1O_2$. Therefore, this indicates that the surface-bound •OH mainly contributes to the $^1O_2$ production by reacting with $O_2^{\bullet-}$/$HO_2^{\bullet}$.

The presence of surface-bound OH can be confirmed by investigating the state of O and H atoms on the surface of FeP by density functional calculation. As shown in Fig. 7e, after relaxation, the H_2O_2 molecule tends to break and form OH on the surface. This strongly indicates that the O and H atoms would preferential exist in the form of adsorbed OH on the surface of the FeP.

The adsorption energy (E) of OH on the FeP is calculated according to the following Eq. (4).

$$E_{ad}=E_{tot}-E_{substrate}-E_{OH} \quad (4)$$

where E_{ad} is the adsorption energy, E_{tot} is the total energy of the molecule on the substrate, $E_{substrate}$ is the energy of the substrate, E_{OH} is the energy of the OH adsorbed.

The calculated adsorption energy of an OH is about − 3.74 eV, which demonstrates that the OH adsorbed on the surface of FeP is thermodynamically favorable.

Therefore, the above results collectively validate that the FeP/TPP system for $^1O_2$ production is a radical-mediated chain reaction (Fig. 8a): Initiated by dioxygen activation (Table S5, Reaction 3), subsequently formed H_2O_2 (Table S5, Reaction 5), then formed •OH via Fenton reaction (Table S5, Reaction 6), and finally formed $^1O_2$ via surface-bound •OH mediated reaction (Table S5, Reaction 11–12). With regarding to the degradation of IBU, $^1O_2$ should mainly contribute to the degradation (64.9%), while other radicals (mainly •OH) account for about 35.1%.

The main intermediate products from the degradation of IBU by FeP/TPP/Air system are also performed (Figure S20). The above experimental results confirmed the co-existence of $^1O_2$ and •OH in FeP/TPP/Air system, and both $^1O_2$ and •OH have the ability to degrade IBU. However, $^1O_2$ is more likely to undergo electrophilic attack,[67] thus, the formation of NO2 and NO3 should be attributed to $^1O_2$ (Figure S20, route 1). NO3 to NO4 is a process of decarboxylation, this should be attributed to •OH. Therefore, the formation of NO4 benefits from the combined effect of $^1O_2$ and •OH. The intermediates produced by •OH are mainly through hydroxylation and decarboxylation process. The process can be seen in route 2 (Figure S20) and route 3 (Figure S20). This result is consistent with the previous reports that •OH attacks can occur at different positions of IBU to produce a variety of hydroxylated products [68,69]. During the degradation of IBU, the degradation route is multiple and the degradation process is complicated. Overall, the effective degradation of IBU in FeP/TPP/Air system is attributed to the combined effect of $^1O_2$ and •OH.

3.6. The versatility and stability of FeP

To investigate the application of the FeP/TPP/Air system for degradation of IBU from real aquatic systems, the degradation experiments are carried out in real water samples, including Pearl River water (PRW), central lake water of Guangzhou University Town (LW) and tap water (TW). Fig. 8b shows the IBU degradation efficiency is unremarkably affected in PRW, LW and TW, indicating that the application of FeP/TPP/Air system in real wastewater remediation is feasible. Moreover, in addition to the anti-inflammatory drug ibuprofen, other organic pollutants, including the antibiotic norfloxacin (NFX), the organic dye methyl blue (MB) and rhodamine B (RhB), can also be degraded effectively in FeP/TPP/Air system (Fig. 8c). These prove that the FeP/TPP/Air system is also feasible for the effective degradation of various organic pollutants.

The stability of FeP is investigated using a cycling experiment. As shown in Fig. 8d, the FeP/TPP/Air system exhibits a high degradation efficiency of IBU within 120 min, even after four cycles. The elementary composition of FeP did not change after four cycles (Figure S21a). Figure S21b shows the identical XRD spectra of fresh and used four cycles of FeP, indicating that the structural stability of the FeP. To further explore the stability of FeP, high-resolution XPS spectra of FeP before and after four cycles are conducted (Fig. 8e and Figure S21c). The peak at 707.2 eV is attributed to the characteristic peak of $Fe^{\alpha+}$ ($0 <$

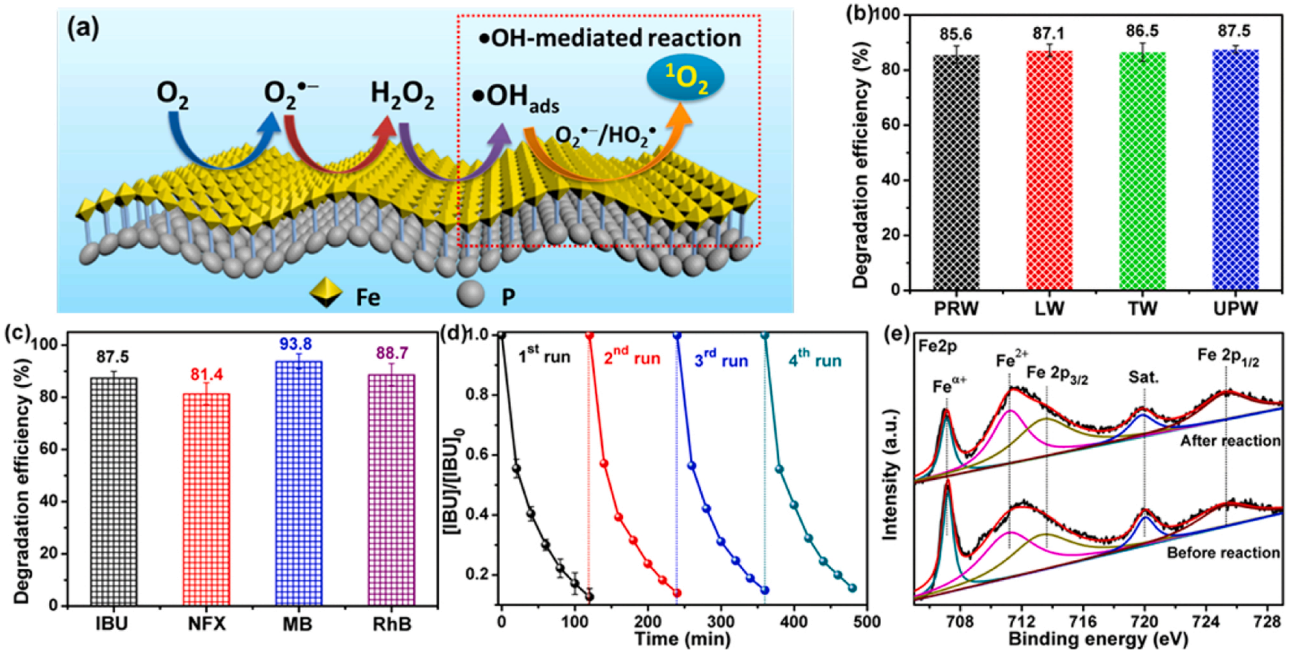

Fig. 8. (a) The reaction mechanism of FeP for $^1O_2$ production. (b) Degradation efficiency of IBU in FeP/TPP/Air system under different real water samples. (c) Degradation efficiency of different organic pollutants in FeP/TPP/Air system. (d) Recycling tests of FeP in IBU degradation. (e) Fe 2p XPS spectra of before and after four cycles of FeP. Reaction conditions: [IBU] = [NFX] = [MB] = [RhB] = 10 ppm; [TPP] = 2 mM; pH = 6.0; [sample] = 0.2 g/L; air-bubbled; reaction time = 120 min.

α + < 2) from FeP, which is similar to that of the metallic state of Fe (706.8 eV).[38,39] The peak at 711.1 eV is ascribed to the Fe^{2+} from the FeP.[24,70] The two peaks located at 713.2 eV and 725.2 eV are ascribed to the typical peaks of Fe $2p_{3/2}$ and Fe $2p_{1/2}$ arising from the oxidation of Fe.[71,72] The peak at 720.0 eV is assigned to the satellite peak.[73] The calculation of the peak area in Fe 2p core-level spectra gives a ratio of $Fe^{\alpha+}/Fe_{total}$, Fe^{2+}/Fe_{total} and Fe^{3+}/Fe_{total} (Table S6). Interestingly, after four cycles, the value of $Fe^{\alpha+}/Fe_{total}$ and Fe^{2+}/Fe_{total} only decreased by 3.7% and 1.6%, respectively. This result indicates that the low valence of $Fe^{\alpha+}$ and Fe^{2+} in FeP still has a robust ability to activate dioxygen by donating electrons after four cycles.

4. Conclusion

In-situ spontaneous production of $^1O_2$ system is green, environment-friendly and practically applicable advanced oxidation technology, since this system does not require light, electricity, and any other oxidants. In this study, FeP is employed as a dioxygen activator for the first time. With the chelation of TPP, FeP could continuously generate $^1O_2$ in aqueous solution for organic pollutants degradation. Combining a series of control experiments, we find that a radical-mediated chain reaction, initiated by dioxygen activation, subsequently formed H_2O_2, and finally formed •OH via Fenton reaction, is crucial for $^1O_2$ production. We further demonstrate that the generated •OH likes to be adsorbed on the FeP surface and then the FeP triggers a surface-bound •OH mediated reaction for $^1O_2$ production. Thus, this finding sheds light on the transformation mechanism from surface-bound •OH to $^1O_2$ and also provides a green application in the field of biology, chemistry and environment. Importantly, this study provides a novel strategy for the application of oxygen gas in the air. Oxygen is widely spread, sustainable, and cost-effective. This method to produce $^1O_2$ by activating oxygen can be extended to many environmental applications such as disinfection and water treatments. The application of FeP in this novel reaction widens and broadens the understanding of iron-based materials and phosphides. New materials with similar structures of FeP could also be explored.

CRediT authorship contribution statement

Ningchao Zheng: Methodology, Conceptualization, Software, Investigation, Resources, Data curation, Writing – original draft. **Xi He:** Formal analysis, Investigation, Resources. **Ruiting Hu:** Investigation. **Ruilin Wang:** Supervision. **Quan Zhou:** Investigation. **Yekai Lian:** Data curation. **Zhuofeng Hu:** Conceptualization, Methodology, Formal analysis, Data curation, Writing – review & editing, Funding acquisition.

Declaration of Competing Interest

The authors declare that they have no known competing financial interests or personal relationships that could have appeared to influence the work reported in this paper.

Acknowledgments

This work is supported by the National Natural Science Foundation of China (Grant No. 51902357), the Natural Science Foundation of Guangdong Province, China (2019A1515012143), the Start-up Funds for High-Level Talents of Sun Yat-sen University (38000-18841209), the Fundamental Research Funds for the Central Universities (19lgpy153) and the Guangdong Basic and Applied Basic Research Foundation (2019B1515120058). The theoretical calculation is supported by National supercomputer center in GuangZhou and National supercomputing center in Shenzhen (Shenzhen cloud computing center).

Appendix A. Supporting information

Supplementary data associated with this article can be found in the online version at doi:10.1016/j.apcatb.2022.121157.

References

[1] H. Kautsky, Quenching of luminescence by oxygen, Trans. Faraday Soc. 35 (1939) 216–219, https://doi.org/10.1039/TF9393500216.
[2] J.L. Cleveland, M.B. Kastan, A radical approach to treatment, Nature 407 (2000) 309–311, https://doi.org/10.1038/35030277.
[3] J.D. Lambeth, NOX enzymes and the biology of reactive oxygen, Nat. Rev. Immunol. 4 (2004) 181, https://doi.org/10.1038/nri1312.
[4] U. Theopold, A bad boy comes good, Nature 461 (2009) 486–487, https://doi.org/10.1038/461486a.
[5] Z. Zhou, J. Song, R. Tian, Z. Yang, G. Yu, L. Lin, G. Zhang, W. Fan, F. Zhang, G. Niu, L. Nie, X. Chen, Activatable singlet oxygen generation from lipid hydroperoxide nanoparticles for cancer therapy, Angew. Chem. Int. Ed. 56 (2017) 6492–6496, https://doi.org/10.1002/anie.201701181.
[6] V. Duarte, D. Gasparutto, L.F. Yamaguchi, J.-L. Ravanat, G.R. Martinez, M.H. G. Medeiros, P.D. Mascio, J. Cadet, Oxaluric acid as the major product of singlet oxygenmediated oxidation of 8-oxo-7,8-dihydroguanine in DNA, J. Am. Chem. Soc. 122 (2000) 12622–12628, https://doi.org/10.1021/ja002218r.
[7] A. Maranzana, C. Canepa, G. Ghigo, G. Tonachini, Theoretical study on the reactivity and regioselectivity of the ene reaction of1Δg O2 with α,β-unsaturated carbonyl compounds, Eur. J. Org. Chem. 2005 (2005) 3643–3649, https://doi.org/10.1002/ejoc.200500215.
[8] J.A. Rengifo-Herrera, K. Pierzchała, A. Sienkiewicz, L. Forró, J. Kiwi, C. Pulgarin, Abatement of organics and Escherichia coli by N, S co-doped TiO2 under UV and visible light. Implications of the formation of singlet oxygen (1O2) under visible light, Appl. Catal. B-Environ. 88 (2009) 398–406, https://doi.org/10.1016/j.apcatb.2008.10.025.
[9] P. Di Mascio, G.R. Martinez, S. Miyamoto, G.E. Ronsein, M.H.G. Medeiros, J. Cadet, Singlet molecular oxygen reactions with nucleic acids, lipids, and proteins, Chem. Rev. 119 (2019) 2043–2086, https://doi.org/10.1021/acs.chemrev.8b00554.
[10] S. Xu, P. Zhou, Z. Zhang, C. Yang, B. Zhang, K. Deng, S. Bottle, H. Zhu, Selective oxidation of 5-hydroxymethylfurfural to 2,5-furandicarboxylic acid using O2 and a photocatalyst of co-thioporphyrazine bonded to g-C3N4, J. Am. Chem. Soc. 139 (2017) 14775–14782, https://doi.org/10.1021/jacs.7b08861.
[11] C. Lu, C. Zhang, P. Wang, Y. Zhao, Y. Yang, Y. Wang, H. Yuan, S. Qu, X. Zhang, G. Song, K. Pu, Light-free generation of singlet oxygen through manganese-thiophene nanosystems for pH-responsive chemiluminescence imaging and tumor therapy, Chem 6 (2020) 2314–2334, https://doi.org/10.1016/j.chempr.2020.06.024.
[12] X. Mi, P. Wang, S. Xu, L. Su, H. Zhong, H. Wang, Y. Li, S. Zhan, Almost 100% peroxymonosulfate conversion to singlet oxygen on single-atom CoN_{2+2} sites, Angew. Chem. Int. Ed. 60 (2021) 4588–4593, https://doi.org/10.1002/anie.202014472.
[13] L. Shi, B. Hernandez, M. Selke, Singlet oxygen generation from watersoluble quantum dot-organic dye nanocomposites, J. Am. Chem. Soc. 128 (2006) 6278–6279, https://doi.org/10.1021/ja057959c.
[14] N. Adarsh, R.R. Avirah, D. Ramaiah, Tuning photosensitized singlet oxygen generation efficiency of novel Aza-BODIPY dyes, Org. Lett. 12 (2010) 5720–5723, https://doi.org/10.1021/ol200572p.
[15] J. Al-Nu'airat, B.Z. Dlugogorski, X. Gao, N. Zeinali, J. Skut, P.R. Westmoreland, I. Oluwoye, M. Altarawneh, Reaction of phenol with singlet oxygen, Phys. Chem. Chem. Phys. 21 (2018) 171–183, https://doi.org/10.1039/c8cp04852e.
[16] S.J. Klebanoff, Myeloperoxidase: friend and foe, J. Leukoc. Biol. 77 (2005) 598–625, https://doi.org/10.1189/jlb.1204697.
[17] J.R. Kanofsky, Singlet oxygen production by biological systems, Chem. Biol. Interact. 70 (1989) 1–28, https://doi.org/10.1016/0009-2797(89)90059-8.
[18] N. Mahne, S.E. Renfrew, B.D. McCloskey, S.A. Freunberger, Electrochemical oxidation of lithium carbonate generates singlet oxygen, Angew. Chem. Int. Ed. 57 (2018) 5529–5533, https://doi.org/10.1002/anie.201802277.
[19] S. Tian, Y. Li, H. Zeng, W. Guan, Y. Wang, X. Zhao, Cyanide oxidation by singlet oxygen generated via reaction between H_2O_2 from cathodic reduction and OCl^- from anodic oxidation, J. Colloid Interf. Sci. 482 (2016) 205–211, https://doi.org/10.1016/j.jcis.2016.07.024.
[20] Q. Chen, H. Wang, C. Wang, R. Guan, R. Duan, Y. Fang, X. Hu, Activation of molecular oxygen in selectively photocatalytic organic conversion upon defective TiO2 nanosheets with boosted separation of charge carriers, Appl. Catal. B Environ. 262 (2020), 118258, https://doi.org/10.1016/j.apcatb.2019.118258.
[21] Z. Liu, H. Ding, C. Zhao, T. Wang, P. Wang, D.D. Dionysiou, Electrochemical activation of peroxymonosulfate with ACF cathode: kinetics, influencing factors, mechanism, and application potential, Water Res. 159 (2019) 111–121, https://doi.org/10.1016/j.watres.2019.04.052.
[22] J. Ji, Q. Yan, P. Yin, S. Mine, M. Matsuoka, M. Xing, Defects on CoS2-x: tuning redox reactions for sustainable degradation of organic pollutants, Angew. Chem. Int. Ed. 60 (2021) 2903–2908, https://doi.org/10.1002/anie.202013015.
[23] W. Xiang, T. Zhou, Y. Wang, M. Huang, X. Wu, J. Mao, X. Lu, B. Zhang, Catalytic oxidation of diclofenac by hydroxylamine-enhanced Cu nanoparticles and the efficient neutral heterogeneous-homogeneous reactive copper cycle, Water Res. 153 (2019) 274–283, https://doi.org/10.1016/j.watres.2019.01.024.

[24] Z. Ai, Z. Gao, L. Zhang, W. He, J.J. Yin, Core-shell structure dependent reactivity of Fe@Fe2O3 nanowires on aerobic degradation of 4-chlorophenol, Environ. Sci. Technol. 47 (2013) 5344–5352, https://doi.org/10.1021/es4005202.

[25] Y. Mu, Z. Ai, L. Zhang, Phosphate shifted oxygen reduction pathway on Fe@Fe2O3 core-shell nanowires for enhanced reactive oxygen species generation and aerobic 4-chlorophenol degradation, Environ. Sci. Technol. 51 (2017) 8101–8109, https://doi.org/10.1021/acs.est.7b01896.

[26] L. Xu, K. Yan, Y. Mao, D. Wu, Enhancing the dioxygen activation for arsenic removal by Cu0 nano-shell-decorated nZVI: Synergistic effects and mechanisms, Chem. Eng. J. 384 (2020), 123295, https://doi.org/10.1016/j.cej.2019.123295.

[27] Q. Yi, J. Ji, B. Shen, C. Dong, J. Liu, J. Zhang, M. Xing, Singlet oxygen triggered by superoxide radicals in a molybdenum cocatalytic fenton reaction with enhanced REDOX activity in the environment, Environ. Sci. Technol. 53 (2019) 9725–9733, https://doi.org/10.1021/acs.est.9b01676.

[28] Z. Yang, J. Qian, A. Yu, B. Pan, Singlet oxygen mediated iron-based Fenton-like catalysis under nanoconfinement, Proc. Natl. Acad. Sci. 116 (2019) 6659–6664, https://doi.org/10.1073/pnas.1819382116.

[29] W.H. Koppenol, Reactions involving singlet oxygen and the superoxide anion, Nature 262 (1976) 420–421, https://doi.org/10.1038/262420a0.

[30] A.U. Khan, M. Kasha, Singlet molecular oxygen in the Haber-Weiss reaction, Proc. Natl. Acad. Sci. 91 (1994) 12365–12367, https://doi.org/10.1073/pnas.91.26.12365.

[31] Y. Zhao, M. Sun, X. Wang, C. Wang, D. Lu, W. Ma, S.A. Kube, J. Ma, M. Elimelech, Janus electrocatalytic flow-through membrane enables highly selective singlet oxygen production, Nat. Commun. 11 (2020) 6228, https://doi.org/10.1038/s41467-020-20071-w.

[32] C. K eenan, D. Sedlak, Factors affecting the yield of oxidants from the reaction of nanoparticulate zero-valent iron and oxygen, Environ. Sci. Technol. 42 (2008) 1262–1267, https://doi.org/10.1021/es7025664.

[33] H.H. Kim, H. Lee, H.E. Kim, J. Seo, S.W. Hong, J.Y. Lee, C. Lee, Polyphosphate-enhanced production of reactive oxidants by nanoparticulate zero-valent iron and ferrous ion in the presence of oxygen: Yield and nature of oxidants, Water Res 86 (2015) 66–73, https://doi.org/10.1016/j.watres.2015.06.016.

[34] L.A. MacManus-Spencer, K. McNeill, Quantification of singlet oxygen production in the reaction of superoxide with hydrogen peroxide using a selective chemiluminescent probe, J. Am. Chem. Soc. 127 (2005) 8954–8955, https://doi.org/10.1021/ja052045b.

[35] X. Li, X. Huang, S. Xi, S. Miao, J. Ding, W. Cai, S. Liu, X. Yang, H. Yang, J. Gao, J. Wang, Y. Huang, T. Zhang, B. Liu, Single cobalt atoms anchored on porous N-doped graphene with dual reaction sites for efficient fenton-like catalysis, J. Am. Chem. Soc. 140 (2018) 12469–12475, https://doi.org/10.1021/jacs.8b05992.

[36] X. Dou, Q. Zhang, S.N.A. Shah, M. Khan, K. Uchiyama, J.M. Lin, MoS2-quantum dot triggered reactive oxygen species generation and depletion: responsible for enhanced chemiluminescence, Chem. Sci. 10 (2019) 497–500, https://doi.org/10.1039/c8sc03511c.

[37] S. Zhu, X. Li, J. Kang, X. Duan, S. Wang, Persulfate activation on crystallographic manganese oxides: mechanism of singlet oxygen evolution for nonradical selective degradation of aqueous contaminants, Environ. Sci. Technol. 53 (2019) 307–315, https://doi.org/10.1021/acs.est.8b04669.

[38] C. Ma, S. Feng, J. Zhou, R. Chen, Y. Wei, H. Liu, S. Wang, Enhancement of H2O2 decomposition efficiency by the co-catalytic effect of iron phosphide on the Fenton reaction for the degradation of methylene blue, Appl. Catal. B Environ. 259 (2019), 118015, https://doi.org/10.1016/j.apcatb.2019.118015.

[39] N. Zheng, X. He, R. Hu, W. Guo, Z. Hu, Co-activation of persulfate by cation and anion from FeP for advanced oxidation processes, Appl. Catal. B Environ. 298 (2021), 120505, https://doi.org/10.1016/j.apcatb.2021.120505.

[40] Z. He, N. Zheng, L. Zhang, Y. Tian, Z. Hu, L. Shu, Efficient inactivation of intracellular bacteria in dormant amoeba spores by FeP, J. Hazard. Mater. 425 (2021), 127996, https://doi.org/10.1016/j.jhazmat.2021.127996.

[41] P. Jiang, Q. Liu, Y. Liang, J. Tian, A.M. Asiri, X. Sun, A cost-effective 3D hydrogen evolution cathode with high catalytic activity: FeP nanowire array as the active phase, Angew. Chem. Int. Ed. 53 (2014) 12855–12859, https://doi.org/10.1002/anie.201406848.

[42] X. Hou, X. Huang, F. Jia, Z. Ai, J. Zhao, L. Zhang, Hydroxylamine promoted goethite surface fenton degradation of organic pollutants, Environ. Sci. Technol. 51 (2017) 5118–5126, https://doi.org/10.1021/acs.est.6b05906.

[43] X. Huang, Y. Chen, E. Walter, M. Zong, Y. Wang, X. Zhang, O. Qafoku, Z. Wang, K. M. Rosso, Facet-specific photocatalytic degradation of organics by heterogeneous fenton chemistry on hematite nanoparticles, Environ. Sci. Technol. 53 (2019) 10197–10207, https://doi.org/10.1021/acs.est.9b02946.

[44] L. Achbergerova, J. Nahalka, Polyphosphate-an ancient energy source and active metabolic regulator, Microb. Cell Fact. 10 (2011) 63, https://doi.org/10.1186/1475-2859-10-63.

[45] H. Sun, J. Wang, Y. Jiang, W. Shen, F. Jia, S. Wang, X. Liao, L. Zhang, Rapid aerobic inactivation and facile removal of escherichia coli with amorphous zero-valent iron microspheres: indispensable roles of reactive oxygen species and iron corrosion products, Environ. Sci. Technol. 53 (2019) 3707–3717, https://doi.org/10.1021/acs.est.8b06499.

[46] C. Zhang, T. Li, J. Zhang, S. Yan, C. Qin, Degradation of p-nitrophenol using a ferrous-tripolyphosphate complex in the presence of oxygen: The key role of superoxide radicals, Appl. Catal. B-Environ. 259 (2019), 118030, https://doi.org/10.1016/J.Apcatb.2019.118030.

[47] Y. Zong, Y. Mao, L. Xu, D. Wu, Non-selective degradation of organic pollutants via dioxygen activation induced by Fe(II)-tetrapolyphosphate complexes: Identification of reactive oxidant and kinetic modeling, Chem. Eng. J. 398 (2020), 125603, https://doi.org/10.1016/j.cej.2020.125603.

[48] H. Kim, J. Lim, S. Lee, H.H. Kim, C. Lee, J. Lee, W. Choi, Spontaneous generation of H2O2 and hydroxyl radical through O2 reduction on copper phosphide under ambient aqueous condition, Environ. Sci. Technol. 53 (2019) 2918–2925, https://doi.org/10.1021/acs.est.8b06353.

[49] X. Zhou, K. Mopper, Determination of photochemically produced hydroxyl radicals in seawater and freshwater, Mar. Chem. 30 (1990) 71–78, https://doi.org/10.1016/0304-4203(90)90062-H.

[50] M.P. Rayaroth, K.P. Prasanthkumar, Y.-G. Kang, C.-S. Lee, Y.-S. Chang, Degradation of carbamazepine by singlet oxygen from sulfidized nanoscale zero-valent iron – citric acid system, Chem. Eng. J. 382 (2020), 122828, https://doi.org/10.1016/j.cej.2019.122828.

[51] N. Chen, H. Shang, S. Tao, X. Wang, G. Zhan, H. Li, Z. Ai, J. Yang, L. Zhang, Visible light driven organic pollutants degradation with hydrothermally carbonized sewage sludge and oxalate via molecular oxygen activation, Environ. Sci. Technol. 52 (2018) 12656–12666, https://doi.org/10.1021/acs.est.8b03882.

[52] S.G. Ardo, S. Nelieu, G. Ona-Nguema, G. Delarue, J. Brest, E. Pironin, G. Morin, Oxidative degradation of nalidixic acid by nano-magnetite via Fe^{2+}/O_2 -mediated reactions, Environ. Sci. Technol. 49 (2015) 4506–4514, https://doi.org/10.1021/es505649d.

[53] A.E. Harvey, J.A. Smart, E.S. Amis, Simultaneous spectrophotometric determination of Iron(ll) and total iron with 1,10-phenanthroline, Anal. Chem. 27 (1955) 26–29, https://doi.org/10.1021/ac60097a009.

[54] N. Chen, Y. Huang, X. Hou, Z. Ai, L. Zhang, Photochemistry of hydrochar: reactive oxygen species generation and sulfadimidine degradation, Environ. Sci. Technol. 51 (2017) 11278–11287, https://doi.org/10.1021/acs.est.7b02740.

[55] M. Jiang, J. Lu, Y. Ji, D. Kong, Bicarbonate-activated persulfate oxidation of acetaminophen, Water Res. 116 (2017) 324–331, https://doi.org/10.1016/j.watres.2017.03.043.

[56] Y. Yin, Y. Ren, J. Lu, W. Zhang, C. Shan, M. Hua, L. Lv, B. Pan, The nature and catalytic reactivity of UiO-66 supported Fe3O4 nanoparticles provide new insights into Fe-Zr dual active centers in Fenton-like reactions, Appl. Catal. B-Environ. 286 (2021), 119943, https://doi.org/10.1016/j.apcatb.2021.119943.

[57] V. Nardello, J. Marko, G. Vermeersch, J.M. Aubry, Mo NMR and kinetic studies of peroxomolybdic intermediates involved in the catalytic disproportionation of hydrogen peroxide by molybdate ions, Inorg. Chem. 34 (1995) 4950–4957, https://doi.org/10.1021/ic00124a007.

[58] J.M. Aubry, Search for singlet oxygen in the decomposition of hydrogen peroxide by mineral compounds in aqueous solutions, J. Am. Chem. Soc. 107 (1985) 5844–5849, https://doi.org/10.1021/ja00307a002.

[59] V. Nardello, S. Bogaert, P.L. Alsters, J.-M. Aubrya, Singlet oxygen generation from H_2O_2/MoO_4^{2-}: peroxidation of hydrophobic substrates in pure organic solvents, Tetrahedron Lett. 43 (2002) 8731–8734, https://doi.org/10.1016/S0040-4039(02)02108-1.

[60] E. Appiani, R. Ossola, D.E. Latch, P.R. Erickson, K. McNeill, Aqueous singlet oxygen reaction kinetics of furfuryl alcohol: effect of temperature, pH, and salt content, Environ. Sci. Process Impacts 19 (2017) 507–516, https://doi.org/10.1039/c6em00646a.

[61] S. Halladja, A. Ter Halle, J.P. Aguer, A. Boulkamh, C. Richard, Inhibition of humic substances mediated photooxygenation of furfuryl alcohol by 2,4,6-trimethylphenol. Evidence for reactivity of the phenol with humic triplet excited states, Environ. Sci. Technol. 41 (2007) 6066–6073, https://doi.org/10.1021/es070656t.

[62] A.M. Braun, H. Dahn, E. Gassmann, I. Gerothanassis, L. Jakob, J. Kateva, C. G. Martinez, E. Oliveros, (2+4)-Cycloaddition with singlet oxygen. ^{17}O-investigation of the reactivity of furfuryl alcohol endoperoxide, Photochem. PhotobioL. 70 (1999) 868–874, https://doi.org/10.1111/j.1751-1097.1999.tb08295.x.

[63] J.D. Laat, H. Gallard, Catalytic decomposition of hydrogen peroxide by Fe(III) in homogeneous aqueous solution mechanism and kinetic modeling, Environ. Sci. Technol. 33 (1999) 2726–2732, https://doi.org/10.1021/es981171v.

[64] A. Ghosh, D.A. Mitchell, A. Chanda, A.D. Ryabov, D.L. Popescu, E.U. Upham, G. J. Collins, T.J. Collins, Catalase-peroxidase activity of iron(III)-TAML activators of hydrogen peroxide, J. Am. Chem. Soc. 130 (2008) 15116–15126, https://doi.org/10.1021/ja8043689.

[65] L. Pan, W. Shi, T. Sen, L. Wang, J. Zhang, Visible light-driven selective organic degradation by FeTiO3/persulfate system: the formation and effect of high valent Fe(IV), Appl. Catal. B Environ. 280 (2021), 119414, https://doi.org/10.1016/j.apcatb.2020.119414.

[66] H. Li, J. Shang, Z. Yang, W. Shen, Z. Ai, L. Zhang, Oxygen vacancy associated surface fenton chemistry: surface structure dependent hydroxyl radicals generation and substrate dependent reactivity, Environ. Sci. Technol. 51 (2017) 5685–5694, https://doi.org/10.1021/acs.est.7b00040.

[67] H. Qian, G. Yu, Q. Hou, Y. Nie, C. Bai, X. Bai, H. Wang, M. Ju, Ingenious control of adsorbed oxygen species to construct dual reaction centers ZnO@FePc photo-Fenton catalyst with high-speed electron transmission channel for PPCPs degradation, Appl. Catal. B Environ. 291 (2021), 120064, https://doi.org/10.1016/j.apcatb.2021.120064.

[68] J. Wang, L. Tang, G. Zeng, Y. Deng, Y. Liu, L. Wang, Y. Zhou, Z. Guo, J. Wang, C. Zhang, Atomic scale g-C_3N_4/Bi_2WO_6 2D/2D heterojunction with enhanced photocatalytic degradation of ibuprofen under visible light irradiation, Appl. Catal. B Environ. 209 (2017) 285–294, https://doi.org/10.1016/j.apcatb.2017.03.019.

[69] X. Li, Y. Wang, S. Yuan, Z. Li, B. Wang, J. Huang, S. Deng, G. Yu, Degradation of the anti-inflammatory drug ibuprofen by electro-peroxone process, Water Res. 63 (2014) 81–93, https://doi.org/10.1016/j.watres.2014.06.009.

[70] Y. Lei, C.S. Chen, Y.J. Tu, Y.H. Huang, H. Zhang, Heterogeneous degradation of organic pollutants by persulfate activated by CuO-Fe3O4: mechanism, stability,

and effects of pH and bicarbonate ions, Environ. Sci. Technol. 49 (2015) 6838–6845, https://doi.org/10.1021/acs.est.5b00623.
[71] Y. Ge, P. Dong, S.R. Craig, P.M. Ajayan, M. Ye, J. Shen, Transforming nickel hydroxide into 3D prussian blue analogue array to obtain Ni2P/Fe2P for efficient hydrogen evolution reaction, Adv. Energy Mater. 8 (2018) 1800484, https://doi.org/10.1002/aenm.201800484.
[72] J. Yan, J. Peng, L. Lai, F. Ji, Y. Zhang, B. Lai, Q. Chen, G. Yao, X. Chen, L. Song, Activation CuFe2O4 by hydroxylamine for oxidation of antibiotic sulfamethoxazole, Environ. Sci. Technol. 52 (2018) 14302–14310, https://doi.org/10.1021/acs.est.8b03340.
[73] B. Zhou, F. Yan, X. Li, J. Zhou, W. Zhang, An interpenetrating porous organic polymer as a precursor for FeP/Fe_2P-embedded porous carbon toward a pH-universal ORR catalyst, ChemSusChem 12 (2019) 915–923, https://doi.org/10.1002/cssc.201802369.